Article

Anisotropy of the ΔE effect in Ni-based magnetoelectric cantilevers: a finite element method analysis

Bernd Hähnlein [1,†,*], Neha Sagar [1,†], Hauke Honig [2,†], Stefan Krischok [1] and Katja Tonisch [1]

[1] Technical Physics 1 Group, Institute of Micro- and Nanotechnologies (IMN MacroNano®), Technische Universität Ilmenau, Postfach 100565, 98684 Ilmenau, Germany; bernd.haehnlein@tu-ilmenau.de (B.H.); neha.sagar@tu-ilmenau.de (N.S.); stefan.krischok@tu-ilmenau.de (S.K.); katja.tonisch@tu-ilmenau.de (K.T.)
[2] Materials for Electronics and Electrical Engineering Group, Institute of Micro- and Nanotechnologies (IMN MacroNano®), Technische Universität Ilmenau, Postfach 100565, 98684 Ilmenau, Germany; hauke-lars.honig@tu-ilmenau.de (H.H.)
* Correspondence: bernd.haehnlein@tu-ilmenau.de (B.H.); katja.tonisch@tu-ilmenau.de (K.T.)
† These authors contributed equally to this work.

Abstract: Magnetoelectric sensors based on microelectromechanical cantilevers consisting of TiN / AlN / Ni are investigated using finite element simulations in regard of the anisotropy of the ΔE effect and its impact on the sensor sensitivity. The ΔE effect is derived from the anisotropic magnetostriction and magnetization of single crystalline Nickel. The magnetic hardening of Nickel in saturation is demonstrated for the (110) as well as the (111) orientation. It is shown further, that magnetostrictive bending of the cantilever has a negligible impact on the eigenfrequency and thus sensitivity. The intrinsic ΔE effect of Nickel decreases in magnitude depending on the crystal orientation when integrated into the magnetoelectric sensor design. The transitions of the individual magnetic domain states are found to be the dominant influencing factor on the sensitivity for all crystal orientations. The peak sensitivity was determined to 41.3 T^{-1} for (110) in-plane orientated Nickel at a magnetic bias flux of 1.78 mT. It is found, that the transition from domain wall shift to domain rotation along the hard axes yields much higher sensitivity than the transition from domain rotation to magnetization reversal. The results achieved in this work show that Nickel as hard magnetic material is able to reach almost identical sensitivities as soft magnetic materials, such as FeCoSiB.

Keywords: delta E effect, magnetoelectric sensor, Nickel, anisotropy

Citation: Hähnlein, B.; Sagar, N.; Honig, H.; Krischok, S.; Tonisch, K.; Anisotropy of the ΔE effect in Ni-based magnetoelectric cantilevers: a finite element method analysis. *Preprints* **2022**, *1*, 0. https://doi.org/

1. Introduction

Magnetic field sensors based on electromechanical systems gained a lot of attraction in the last decade as the magnetoelectrical sensor concept exhibits promising device characteristics enabling the detection of weakest magnetic fields as needed for example in biomedical applications or geophysical explorations. In this kind of sensors, the ΔE effect, which describes the change of the Young's modulus in presence of a magnetic field, is the basic physical property utilized in this sensor concept. High sensitivities and low limits of detection in the low $pT/\sqrt{Hz}$ regime [1–3] have been realized in the last decade paving the way down to the $fT/\sqrt{Hz}$ range at room temperature [4] where usually only superconducting quantum interference devices (SQUID) [5] could be used. Magnetoelectric sensors exhibit the great advantage, that in contrast to SQUIDs no extensive cooling is required to achieve their superconducting state for operation, leading to less complex and costly operation. Currently, common magnetoelectric sensors exhibit sizes in the millimeter [3,6,7] up to centimeter range [8–10] and are usually based on amorphous soft magnetic materials, for example FeCoSiB [11], FeGaB [12] or Terfenol-D [2], in combination with a piezoelectric material for the output signal generation, like AlN [12], PZT [13] or metglass [14]. Comparably few references can be found that target sensors in the microelectromechanical system (MEMS) regime [15–17], a highly interesting transition region where anisotropic material properties show increasing influence on the device characteristics when the sensor dimensions start to reach the order of magnitude of single crystals within the (poly-)crystalline material [18,19]. Besides the anisotropy size effects also play a role in the MEMS regime,

Preprints (www.preprints.org) | NOT PEER-REVIEWED | Posted: 27 May 2022 doi:10.20944/preprints202205.0373.v1

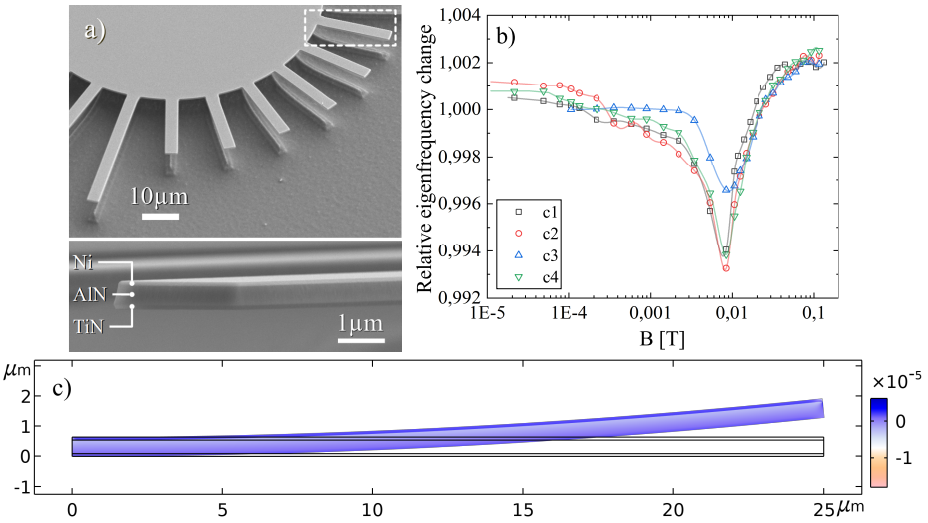

Figure 1. a) SEM images of 4 µm wide magnetoelectric cantilevers consisting of a TiN(90 nm)/AlN(450 nm)/Ni(100 nm) layer stack investigated in recent work [19]. b) Eigenfrequency characteristics in dependency of the magnetic flux of four 25 µm long and identically aligned cantilevers as marked in a). c) Solution of the 2D model used for the simulation study with the layer configuration from a). The bending effect due to magnetostrictive strains in the 25 µm cantilever is up-scaled for better visibility.

e.g. the Young's modulus [20] and magnetization [21] of Nickel or the piezoelectric layer [22,23].

In magnetoelectric sensors Nickel is often used in combination with a second magnetostrictive material to realize magnetization-graded structures for the optimization of the magnetoelectric coupling [24,25]. In the MEMS regime, where the structure dimensions are converging to the magnetic domain size, the magnetic or magnetoelectric properties can be predominantly described by a single crystalline magnetostrictive material. Recently, anisotropy effects in pristine TiN/AlN/Ni sensors have been investigated showing sensitivities comparable to other sensors based on soft magnetic materials though the sensor volume in total is several orders of magnitude lower (see Fig. 1 a) and b)) [19]. The polycrystalline nature of the analysed Nickel layer affects the sensor performance in a way, that the orientation of its crystallites is statistically distributed to a certain extent. To investigate the intrinsic potential of Nickel as magnetostrictive material, the anisotropic properties and the respective dependency on the layer thickness are analysed within a finite element study.

2. Modelling the sensor

2.1. Model details

For the investigation of the vibrational behaviour with Comsol 5.6 (Comsol Multiphysics GmbH, D-37073 Göttingen, Germany) a 2D model with coupled multiphysics (solid mechanics and magnetostriction) was chosen since the requirements for a 3D model demand two orders of magnitude higher memory usage and calculation time at still lower mesh quality. However, this limits the possibility to analyse effects arising from the complex geometry of experimental structures, like the influence of the undercut impacting on the eigenfrequency, especially at shorter cantilevers [18], a non-rectangular cross section or complex (thermal) stress profiles in the clamping region. The 2D model is otherwise based on the recently investigated magnetoelectric sensors [19] shown in Fig. 1 a). The basic sensor design consists of the length $l_c = 25$ µm, width $w_c = 4$ µm and a multilayer structure consisting of TiN (90 nm), AlN (450 nm) and Ni on top with varying thickness $t_{Ni} = 100$-1000 nm. A stationary solution for the magnetostriction related bending of a cantilever with $t_{Ni} = 100$ nm is shown in Fig. 1 c) for comparison. The layers are modeled

Preprints (www.preprints.org) | NOT PEER-REVIEWED | Posted: 27 May 2022 doi:10.20944/preprints202205.0373.v1

as single crystals and effective medium to be able to study the different effects from the point of a most general (ideal) case. This allows to study the intrinsic anisotropic behavior of Nickel while minimizing the influence of the specific sensor design which has usually a high impact on the device performance. Further parameters used for the simulation are summarized in Appendix A.

2.2. ΔE effect of Nickel

Magnetostriction in general describes the structural response of the lattice of a magnetic material to the change of an external magnetic field. The magnetic domains in ferromagnetic materials like Nickel are randomly oriented in the unmagnetized state, each with saturation magnetization M_s. In presence of a magnetic field, the minimization of the internal energy leads to the alignment of the domains along the field direction. In isotropic materials the rotation of magnetization by an angle θ causes magnetostrictive strain λ [26]

$$\lambda = \frac{3}{2}\lambda_s cos^2\theta - \frac{1}{3}, \tag{1}$$

with λ_s as the isotropic saturation magnetostrictive strain. In the anisotropic case, the magnetostriction is depending on the principal axes (hkl) of the materials lattice. The magnetostriction is thus given (and used by Comsol) by

$$\lambda_{hkl} = \frac{3}{2}\lambda_{100}\left(\sum_{i=1}^{3} m_i^2\psi_i^2 - \frac{1}{3}\right) + 3\lambda_{111}\left(\sum_{i,j=1}^{3} \vec{m}_i\vec{m}_j\psi_i\psi_j\right), \tag{2}$$

with $i \neq j$ and cyclic permutation. Here, $\psi_{i,j}$ is the angle cosine of the respective direction in relation to $\vec{M}$ and $\vec{m_{i,j}}$ the direction vector $\vec{M}/M_s$. Within Eq. 2 volume conservation is assumed. Other effects breaking the volume conservation like the volume magnetostriction [27] are thus not considered. The magnetostriction constants of Nickel are all negative [28] leading to compression strains along the three principal axes. The experimental curves are given in Appendix B with their respective fits. The curve for the (110) direction is also presented for completeness, though not needed according to Eq. 2. As the curve fits exhibit an increasing error for $H < 1000\,\mathrm{A/m}$, the discussion of the sensor characteristics in section 3 is limited to $B > 1\,\mathrm{mT}$.

The development of magnetically induced strains λ_{hkl} in a magnetostrictive material results in a change of the Young's modulus, the so-called ΔE effect. It can be described analytically [29], so that

$$\frac{1}{E_{hkl}} = \frac{\partial(\epsilon_{hkl} + \lambda_{hkl})}{\partial\sigma_{hkl}} = \frac{1}{E_{hkl,sat}} + \frac{1}{\Delta E_{hkl}}, \tag{3}$$

while ΔE_{hkl} is directly depending on the derivations of λ_{hkl} and the magnetization M_{hkl}:

$$\frac{1}{\Delta E_{hkl}} = \frac{(\partial\lambda_{hkl}/\partial H)^2}{\mu_0\partial M_{hkl}/\partial H}. \tag{4}$$

The static inverse elastic modulus $1/E_{hkl,sat}$ of the cubic Nickel lattice in Eq. 3 can be calculated using the compliance matrix S_{ii} and the direction cosines α, β and γ by [30]:

$$\frac{1}{E_{hkl,sat}} = S_{11} - (2(S_{11} - S_{12}) - S_{44})(\alpha^2\beta^2 + \alpha^2\gamma^2 + \beta^2\gamma^2). \tag{5}$$

The tensor elements of the compliance matrix for Nickel are derived from literature values [31] and averaged to $S_{11} = 7.47 \times 10^{-12}\,\mathrm{Pa}^{-1}$, $S_{12} = -2.84 \times 10^{-12}\,\mathrm{Pa}^{-1}$ and $S_{44} = 8.33 \times 10^{-12}\,\mathrm{Pa}^{-1}$ (see Appendix B). The resulting Young's moduli for the three directions in saturation are $E_{100,sat} = 134\,\mathrm{GPa}$, $E_{110,sat} = 228\,\mathrm{GPa}$ and $E_{111,sat} = 297\,\mathrm{GPa}$, respectively. The Poisson ratios for the single crystalline Nickel derived from the elastic constants equal $\nu_{(\langle1,0,0\rangle),(\langle0,1,0\rangle)} = 0.381$, $\nu_{(\langle1,1,0\rangle),(\langle1,\bar{1},0\rangle)} = -0.06$ and $\nu_{(\langle1,1,1\rangle),(\langle1,\bar{1},0\rangle)} = 0.142$.

Preprints (www.preprints.org) | NOT PEER-REVIEWED | Posted: 27 May 2022 doi:10.20944/preprints202205.0373.v1

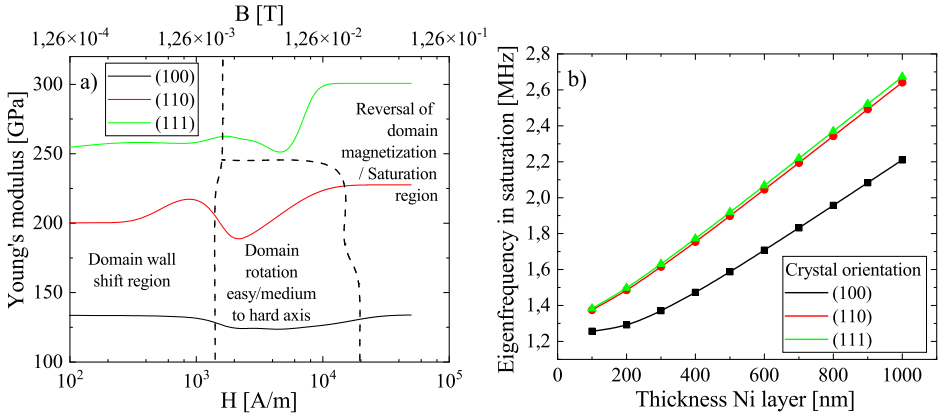

Figure 2. a) Computed magnetic field dependent curves of the Young's modulus for the three principal axes. b) Eigenfrequencies of the simulated cantilevers in magnetic saturation as a function of the crystalline orientation of the Nickel layer and its thickness.

$\nu_{(\langle 1,0,0\rangle),(\langle 0,1,0\rangle)}$ is thus higher than reported values for other single crystals (0.315-0.329) [32] or nanowires (0.305-0.335) [33].

In the cubic crystal different transitions are passed through during magnetization. For low fields domain wall shifts appear which are followed by the domain rotation out of the easy axis towards the external magnetic field direction, eventually followed by the magnetization reversal of anti-parallel oriented domains and saturation. In Nickel, the (111) direction is the easy axis and the (110) and (100) directions are the medium and hard axes, respectively. This is depicted in Fig. 2 a) in combination with the derived Young's moduli E_{hkl} according to Eq. 3. The domain wall shift region is beyond the accurate fit limit why an investigation in this range is not possible with the given data. The domain rotation region describes the reorientation of the domains along the hard axis and exists only for the hard axes of magnetization. The transition from the wall shift to the domain rotation introduces a decrease in $E_{100/110}$ with a distinct minimum at around 2 mT. At higher fluxes, $E_{100/110}$ increases again and reaches a maximum in the saturation region. The easy axis is in contrast characterized by the direct transition from domain wall shifts to magnetic domain reversal as the magnetic domains are already aligned along (111). This leads to a rather flat dependency up to the point where saturation happens at $H > 6000\,\mathrm{A/m}$. This is accompanied by a strong increase in the Young's modulus, the known effect of magnetic hardening. This is also observable for the (110) direction while it has to be noted, that the (100) direction exhibits no such hardening, i.e. $E_{100,0} = E_{100,sat}$. Not only the shape of the ΔE effect is direction dependent but also the magnitude. In (100) direction the maximum change of the Young's modulus $E_{100,min}/E_{100,sat}$ is 7.5 %. The other two directions exhibit a much higher change of 17 % each which is similar to the reported value of 20 % [34]. Observations in Nickel nano crystals revealed even increases of 31 % along (111) [34], nearly twice as high than the calculated increase in this work. Further investigations are needed at this point to check whether such increases appear also in polycrystalline Nickel layers.

3. Results

The calculated natural eigenfrequencies in magnetic saturation for the cantilevers with different crystal orientations of the Nickel layer are given in Fig. 2 b). In accordance to the change in $E_{hkl,sat}$ for the respective directions, the eigenfrequencies show the expected increase when rotating the crystal orientation away from (100). For low thicknesses t_{Ni}, the eigenfrequencies converge to the natural frequency of the residual layer stack of TiN/AlN. Above approximately 300 nm in case of (100)-Ni and 200 nm for (110)/(111)-Ni the eigenfrequencies scale linearly. The simulated eigenfrequencies are 20-30 % higher than the respective experimental eigenfrequencies [19] of the structures in Fig. 1 a), on

Preprints (www.preprints.org) | NOT PEER-REVIEWED | Posted: 27 May 2022 doi:10.20944/preprints202205.0373.v1

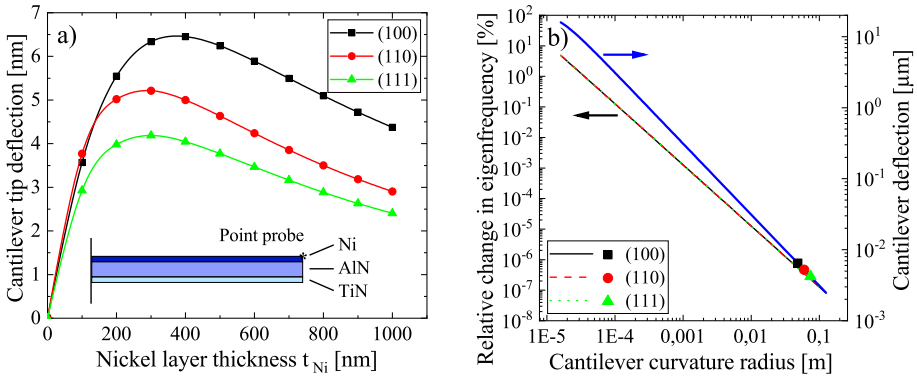

Figure 3. a) Deflection in magnetic saturation of the simulated cantilever for different thicknesses t_{Ni}. b) Influence of the cantilever curvature on the eigenfrequency. The curvature caused by magnetostriction is derived for comparison from a).

which the model is based. Main reason is the undercut that has been neglected in the simulation which can lead to a frequency shift in the range of 20 % [18] or even higher, depending on the undercut depth. A second important influencing factor is the single crystal approximation of the individual layers in contrast to the experimental data.

3.1. Magnetostriction and bending

In presence of a magnetic field, the magnetostriction λ_{hkl} in Eq. 3 applies stresses to the Nickel layer and hence to the adjacent AlN resulting in a bending of the cantilever. As λ_{hkl} is always negative in Nickel, cantilevers are bent upwards for the modelled stacking order, regardless of the crystalline orientation. The magnetostriction induced tip deflection is presented in Fig. 3 a) for the three orientations and different thicknesses t_{Ni}.

The dependencies follow in general the magnetostriction curves in Appendix B, where the (100) direction exhibits the largest strain and the (111) direction the lowest. The tip deflection is maximized at 400 nm for (100) and at 300 nm for (110)/(111) orientation and thus at the same t_{Ni} where the linear eigenfrequency region in Fig. 2 b) begins. Further increase of t_{Ni} leads to a decrease of the deflection which is caused by the shift of the neutral axis towards the Nickel layer within the cantilever, leading to a decrease of the bending moment. The absolute deflection is in the range of 4-6.5 nm which is small compared to the total thickness of the cantilever of around 1 µm. The curvature of a cantilever has influence on its eigenfrequency behaviour. This consideration is important for parameter extraction, where the Euler-Bernoulli theory is used [18]. Here, the eigenfrequencies i of a cantilever are given by

$$f_{i,c} = \frac{\varkappa_i'^2}{2\pi {l_c}^2}\sqrt{\frac{(EI)_{tot}}{(\rho A)_{tot}}}, \tag{6}$$

with $\varkappa_i'$ as the curvature dependent eigenvalue, $(EI)_{tot}$ as the bending stiffness of the multilayer stack and $(\rho A)_{tot}$ as the reduced mass. $\varkappa_i'$ is calculated by [35]

$$\varkappa_i'^2 = \sqrt{\varkappa_i^4 + c\vartheta_i^4}, \tag{7}$$

with $c = (l_c/r)^2$ as the curvature coefficient where r is the curvature radius and ϑ_i as the curvature correction term given by $\vartheta_i^4 = (p_1 + p_2 k)/(p_3 + p_4 k)$ where $k = Al_c^2/I$. For the analysis of the impact of the cantilever deflection according to Fig. 3 a) on its natural mode ($i = 1$) in Fig. 2 b), the respective parameters are set to $\varkappa_1 = 1.875$, $p_1 = 0.7365$, $p_2 = -0.5017$, $p_3 = 1.215$ and $p_4 = -1$. The curvature dependent change in the eigenfrequency $f_{i,c}/f_{i,0}$ is presented in Fig. 3 b). The respective parameters in Eq. 6 are taken from the model parameters in saturation. Interestingly, the relative impact on the eigenfrequency is not directly depending on the Nickel crystal orientation, but only on the curvature

Preprints (www.preprints.org) | NOT PEER-REVIEWED | Posted: 27 May 2022 doi:10.20944/preprints202205.0373.v1

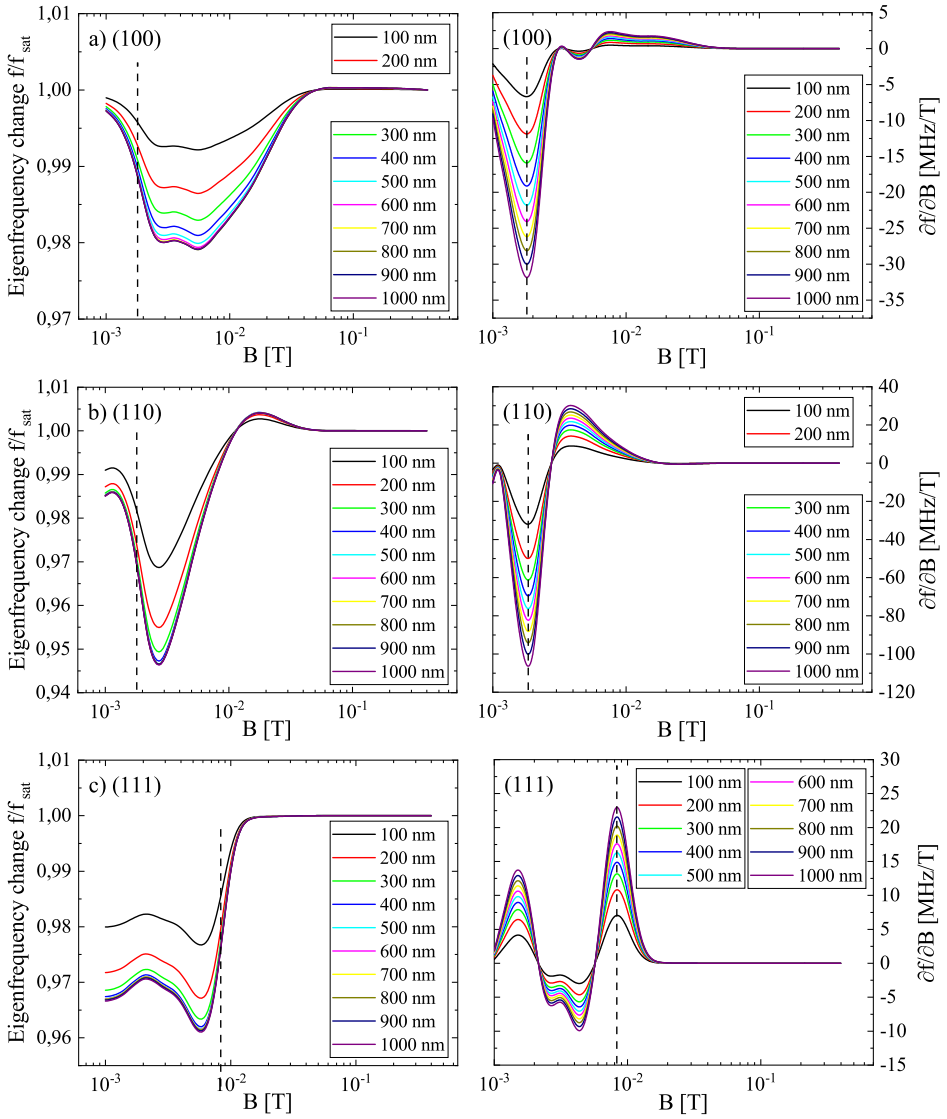

Figure 4. Relative eigenfrequency change f/f_{sat} (left hand side) and the respective specific sensitivity $\partial f/\partial B$ (right hand side) of the three principal axes a) (100), b) (110) and c) (111) for Nickel layer thicknesses t_{Ni} in the range of 100-1000 nm. The point of highest absolute sensitivity is marked by the line, respectively.

radius. Assuming a circular arc, the deflection is coupled with the curvature radius by $\delta = r(1 - cos(l_c/r))$. This dependency is also plotted in Fig. 3 b) along with the maximum deflections gathered from Fig. 3 a). The curvature resulting from magnetostriction alone is very small and the curvature radius comparably large. Consequently, the relative change in eigenfrequency is also very small for any crystal orientation, while for (100) the highest and for (111) the lowest deviation can be observed. The difference between the directions is approximately 24 % having almost no effect at such low radii. However, if a pre-stressed cantilever is given with a static radius much smaller than 0.1 m as shown in thin AlN layers [22], the anisotropic effect of the crystal orientation should be considered in the bending correction of the eigenfrequency in Eq. 6.

3.2. Eigenfrequency behaviour in the magnetic field

The derivation of E_{hkl} as isotropic parameter and the neglect of stress affecting the magnetization $\partial\sigma/\partial M$ and the magnetostriction $(\epsilon_{hkl} + \lambda_{hkl})$ leads in general to the reproduction of E_{hkl} from Fig. 2 a) in the respective eigenfrequency change f/f_{sat}. These

Preprints (www.preprints.org) | NOT PEER-REVIEWED | Posted: 27 May 2022 doi:10.20944/preprints202205.0373.v1

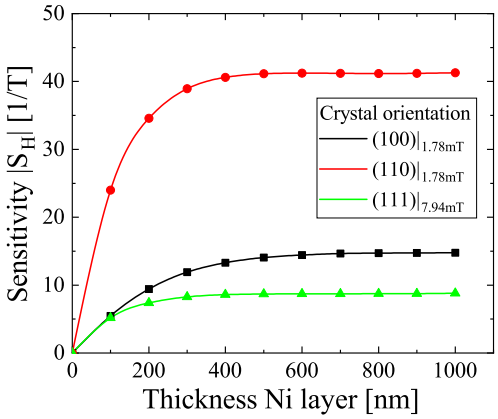

Figure 5. Absolute values of the maximum sensitivities derived from Fig. 4 for the three principal axes at the given offsets of the magnetic flux. Maximum sensitivity and the saturation layer thickness $t_{Ni,sat}$ vary with the orientation. The value for zero thickness is extrapolated.

changes are depicted in Fig. 4 as well as the respective specific sensitivities $\partial f/\partial B$ for each crystal orientation for different thicknesses t_{Ni}. Independent on the orientation, increasing thickness is resulting in an increase of the magnitude of the ΔE effect, which is saturating at specific thicknesses for the individual orientations. Due to the additional functional layers in the sensor design, the magnitude is lower in total than in the pristine ΔE curves of Fig. 2 a). As a consequence, in (100) orientation the magnitude is reduced from 7.5 % to 2.1 % while the (110) and (111) oriented Nickel is reduced from 17 % to 5.4 % and 4 %, respectively. This decrease in the magnitude affects also the sensitivity and can not be avoided in a magnetoelectric MEMS device, but only minimized by design optimization. The specific sensitivity $\partial f/\partial B$ shows a similar dependency between the hard axes with an identical absolute sensitivity maximum at 1.78 mT. This maximum is related to the transition from domain shift to domain rotation and thus is not observable for the easy axis. The local maximum of (111) oriented Nickel at approximately 1.5 mT is originating from a steeper slope of the magnetostriction at this point and strongly depending on the fitting accuracy in this approach. In contrast to the visual appearance of the f/f_{sat} curves, $\partial f/\partial B$ is absolutely much higher in the transition from domain shift to rotation at 1-2 mT than for the transition from domain rotation to magnetization reversal at >2 mT. The difference in $\partial f/\partial B$ is an order of magnitude for (100) while for (110) it is a factor of approximately 3. That is, $\partial f/\partial B$ is mainly driven by $(\partial\lambda_{hkl}/\partial H)^2$ for the hard axes and less depending on the regime of magnetization reversal. For (111) oriented Nickel, the highest $\partial f/\partial B$ can be found at the magnetization reversal transition as expected from the f/f_{sat} curve.

The sensitivity of a magnetoelectric, mechanical sensor, e.g. singly clamped cantilevers or doubly clamped beams, is usually described by the normalized $\partial f/\partial B$:

$$S_H = \frac{1}{f_{sat}}\frac{\partial f}{\partial B}. \tag{8}$$

In Fig. 5 the peak sensitivities of the three principal axes of Nickel are presented in dependency of t_{Ni}. For the given simulation model all orientations exhibit a saturation behaviour with different saturation thicknesses and saturation sensitivities. The saturation thicknesses are depending on the specific layer configuration in terms of materials chosen for the back electrode and the piezoelectric material as well as their respective thicknesses. For the given stack of 90 nm TiN and 450 nm AlN the saturation thicknesses are approximately 500 nm, 400 nm and 300 nm for (100), (110) and (111) and appear to scale anti-proportionally with E_{hkl}. The saturation region is strongly depending on the stresses and the internal magnetic stray field of the magnetostrictive layer. This can result in a decrease of the sensitivity at increasing thicknesses [11]. In soft magnetic materials with usually positive magnetostriction, like the frequently used amorphous FeCoSiB [36],

Preprints (www.preprints.org) | NOT PEER-REVIEWED | Posted: 27 May 2022 doi:10.20944/preprints202205.0373.v1

FeGaB [37] and Terfenol-D [38], internal strains (e.g. stress gradients arising from layer growth) lead to a decrease of the ΔE effect according to Eq. 3. However, such strains can be minimized or tuned experimentally via a DC offset applied to the piezoelectric layer [39] or by using a symmetric sensor design. A great benefit of Nickel in this case are the negative saturation magnetostriction constants for all axes. Nickel grows typically tensile strained on AlN layers leading to potentially increased magnetostriction [40] and thus ΔE effect. Similarly, this was used to optimize the sensor performance on basis of FeCoSiB [41]. In an otherwise unstressed cantilever magnetostrictive bending has negligible influence on the eigenfrequency and thus sensitivity. The magnetic stray field as the second influencing factor affects the sensor performance when vertical domain separation occurs, which is usually negligible within the thin layers of MEMS structures. For comparison the domain wall size in Nickel is approximately 125 nm [42] with typical domain sizes of approximately 200 nm in the unmagnetized state at room temperature [43]. Consequently, the saturation regime in Fig. 5 should be a good estimation of real sensors.

Table 1. Comparison of simulated and experimental sensitivities of the natural frequency of electromechanical system based magnetoelectric sensors. (Values calculated according to Eq. 8 if not given in the reference). * Sensitivity for the second eigenmode.

Material	Reference	Sensitivity [1/T]
Ni(100)/AlN/TiN^{sim}	this work	-14.9
Ni(110)/AlN/TiN^{sim}	this work	-41.3
Ni(111)/AlN/TiN^{sim}	this work	8.8
poly-Ni/AlN/TiN^{exp}	[19]	-0.9 ... -1.4
FeCoSiB/poly-Si/AlN^{exp}	[11]	10
FeCoSiB/poly-Si/AlN^{exp}	[11]	13*
FeCoSiB/poly-Si/AlN^{sim}	[11]	48*
FeCoB/Al/AlN/Pt^{exp}	[16]	-0.7
FeGaB/AlN/Pt^{exp}	[44]	-2.2
FeGa/Ti/Diamond^{exp}	[17]	0.5

In Table 1 the extracted peak sensitivities are summarized in comparison with experimentally derived sensitivities of the structures in Fig. 1 a) and b) as well as of magnetoelectric sensors based on other material combinations. A clear gap is visible in the experimentally realized sensors compared to the theoretical expectations. The recently measured sensitivity of hard magnetic poly-crystalline Ni/AlN/TiN sensors lies in the order of 1 T^{-1} which is comparable to other references based on soft magnetic FeGa or FeCo compounds. Sensors based on FeCoSiB are able to reach higher sensitivities by a factor of 5-10 in combination with a high degree of optimization. The theoretical results remain still significantly higher but are similar between soft magnetic FeCoSiB and the (110) oriented Nickel. The given simulated FeCoSiB sensitivity of 48 T^{-1} is obtained for the second bending mode which yields a higher value than the first/natural mode. The first bending mode should yield a sensitivity approximately 20 % lower according to the data [11] leading to an almost identical result as Ni(110). The direct growth of (110) in-plane oriented Nickel is experimentally difficult on a hexagonal substrate like AlN. However, there are approaches using 150 nm thick Au/Ge interfacial layers [10] for larger sensors. Additional interface engineering is needed to see, whether this configuration can be scaled down to MEMS structures. Further similarities between FeCoSiB and Nickel apply to the saturation magnetostriction [45] or the density [46] leading to a similar mass inertness in the vibrational behavior, e.g. in passive operation. However, MEMS structures are less suitable for passive operation due to the size dependence of the limit of detection [47]. In actively operated sensors, the limit of detection plays a negligible role why the sensitivity is the figure of merit to be used. On basis of the presented results a step wise integration of experimental conditions can be realized in further studies, for example in

 doi:10.20944/preprints202205.0373.v1

terms of poly-crystallinity, stresses or design related changes. The knowledge gained in the MEMS regime might also help understanding and optimizing larger sensors.

4. Conclusion

In this work the anisotropic ΔE effect of Nickel was used to study its influence on the sensitivity of a magnetoelectric sensor within a finite element simulation approach based on recent experimental results and to evaluate the intrinsic potential of this hard magnetic material. For the three principal axes of the fcc lattice the anisotropic Young's modulus of single crystalline Nickel was derived from the direction dependent magnetostriction and magnetization and its elastic constants. It could be shown, that the resulting magnetic field dependency of the Young's modulus is highly depending on the orientation of the crystal and the different transitions between domain wall shift, rotation and the reversal of magnetization. As a result, the known magnetic hardening effect of Nickel could be reproduced field dependent for the (110) hard axis and the (111) easy axis in in-plane orientation while the (100) hard axis does not exhibit this effect. The magnitude of the intrinsic ΔE effect of Nickel is anisotropic and peaks at 7.5 % for (100) and at 17 % for (110) and (111) orientation, respectively. Within the sensor, the ΔE effect magnitude decreases to 2.1 % for the (100), 5.4 % for (110) and 4 % for (111) orientation. The magnetostriction induced bending of the cantilever was investigated to determine its impact on the eigenfrequency. It was shown, that magnetostriction alone has negligible influence on the eigenfrequency. The impact of the different transitions in the magnetic field on the eigenfrequency and on the sensitivity showed, that the transition from the domain wall shift to the domain rotation in the hard axes directions leads to a strong sensitivity, especially along (111) yielding S_H =41.3 T^{-1} at a magnetic bias flux of 1.78 mT. Such high sensitivity is nearly identical to frequently used soft magnetic materials, like FeCoSiB. However, the comparison between simulation and the experimental results indicates, that there is still a high potential for further optimizations of the sensor performance, regardless of the used materials.

Author Contributions: B.H.: Software, Methodology, Formal analysis, Investigation, Writing (Original draft); N.S.: Software, Methodology, Formal analysis, Investigation; H.H.: Methodology, Formal analysis, Investigation; S.K.: Writing (review and editing), Project administration, Supervision, Funding acquisition; K.T.: Writing (review and editing), Project administration, Funding acquisition. All authors have read and agreed to the published version of the manuscript.

Funding: This work was supported in part by the Free State of Thuringia and the European Social Fund (2017 FGR 0060) within the research group "MagSens - Ultrasensitive Magnetfeldsensorik mit resonanten magnetoelektrischen MEMS".

Data Availability Statement: Additional data is available on request from the authors.

Conflicts of Interest: The authors declare no conflict of interest.

Appendix A

The mesh is adjusted to the respective layers with a quad mesh for TiN (mesh size of 106250 elements), a triangular mesh for AlN (mesh size of 276812 elements) and a quad mesh for Nickel (mesh size of 100000 elements). The maximum element size within the Nickel layer is tied to the thickness by $t_{Ni}/20$. The minimum element quality is > 0.5. The model is solved using a linear, fully coupled (stationary and eigenfrequency), direct MUMPS solver with tolerances $\leq 10^{-6}$. The polycrystalline nature of the TiN layer is considered using a reduced Young's modulus of 250 GPa [48].

Appendix B

The magnetostriction and magnetization curves are taken from literature [28,49] and fitted according to [50]

Preprints (www.preprints.org) | NOT PEER-REVIEWED | Posted: 27 May 2022 doi:10.20944/preprints202205.0373.v1

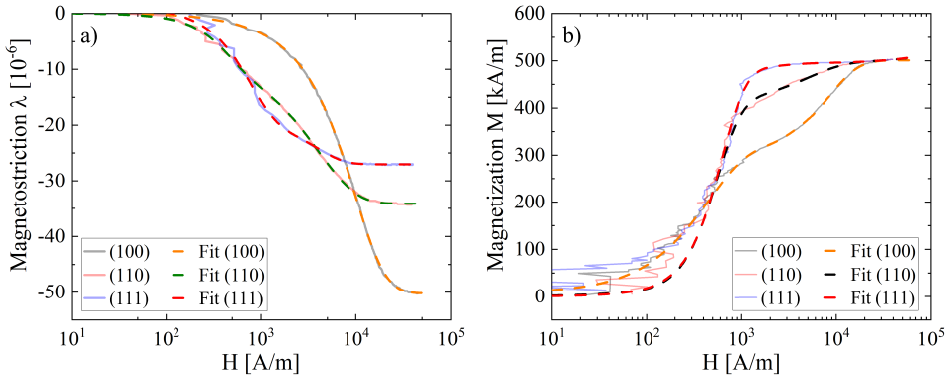

Figure A1. a) Experimental magnetostriction curves of Nickel taken from [28] and their respective fits for the three principal axes. b) Experimental magnetization curves of Nickel taken from [49] and their respective fits of the dependency of the magnetic field.

$$\lambda_{hkl}(H) = \sum_i \kappa_{hkl,sat,i}\left(1 - \frac{3}{cosh(\alpha_i(H - H_{0,i})) + 2}\right). \tag{A1}$$

The extracted curves as well as the fits are presented in Fig. A1 for $i = 2$. The given formula for $M(H)$ in [50] is not able to reproduce the magnetization curve accurately enough. Therefore, Eq. A1 is used here also to minimize the fitting error since $\partial M/\partial H$ is highly sensitive for deviations and thus the derived ΔE effect in Eq. 5. The determined constants are given in Table A1.

Table A1. Fit constants for the magnetostriction and magnetization curves according to Eq. A1.

Parameter	$\kappa_{hkl,sat,1}$	$\kappa_{hkl,sat,2}$	α_1 **[10^{-4} m/A]**	α_2 **[10^{-4} m/A]**	$H_{0,1}$ **[A/m]**	$H_{0,2}$ **[A/m]**
λ_{100}	$-1.61\cdot10^{-5}$	$-1.34\cdot10^{-4}$	2.17	1.40	0	-22132
λ_{110}	$-7.95\cdot10^{-6}$	$-1.27\cdot10^{-4}$	-52.4	2.80	0	-11500
λ_{111}	$-2.24\cdot10^{-5}$	$-7.16\cdot10^{-6}$	-26.2	-5.35	-200	-500
M_{100}	260000	276100	-2.08	9.43	-5000	0
M_{110}	403234	248314	42.8	-2.50	0	-10000
M_{111}	10621	483372	8.86	37.9	0	0

Preprints (www.preprints.org) | NOT PEER-REVIEWED | Posted: 27 May 2022 doi:10.20944/preprints202205.0373.v1

Table A2. Summary of the elastic constants of Ni gathered from [31]. *Omitted values due to high deviation.

Reference	C_{11} $[10^{11} Pa]$	C_{12} $[10^{11} Pa]$	C_{44} $[10^{11} Pa]$
Honda et al.	2.52	1.51	1.04
Bozorth1 et al.	2.5	1.6	1.19
Bozorth2 et al. Saturated	2.52	1.57	1.23
Neighbours et al.	2.53	1.52	1.24
Yamamoto et al.	2.44	1.58	1.02
Levy et al.	2.47	1.52	1.21
DeKlerk et al. Saturated	2.46	1.47	1.24
Shirakawa et al.	2.55	1.69	0.90*
DeKlerk2 et al. Saturated	2.46	1.48	1.22
Alers et al.	2.51	1.5	1.24
Sakurai et al.	2.51	1.53	1.24
Epstein et al. Saturated	2.5	1.54	1.24
Vintaikin et al.	2.47	1.44	1.24
Salama et al.	2.52	1.54	1.22
Shirakawa2 et al.	2.88	1.81	1.24
Average	**2.52**	**1.55**	**1.2**

The angle cosines for the fcc lattice of Nickel are $(\alpha, \beta, \gamma)_{100} = (1, 0, 0)$ as well as $(1/\sqrt{2}, 1/\sqrt{2}, 0)$ and $(1/\sqrt{3}, 1/\sqrt{3}, 1/\sqrt{3})$ for the (110) and (111) direction, respectively. The compliance matrix is derived from the literature values given in [31] and summarized in Table A2. The tensor elements S_{ii} of the compliance matrix C_{ii} are subsequently derived from the stiffness matrix elements using the well known formulas

$$\begin{aligned} S_{11} &= \frac{C_{11} + C_{12}}{(C_{11} - C_{12})(C_{11} + 2C_{12})}, \\ S_{12} &= -\frac{C_{12}}{(C_{11} - C_{12})(C_{11} + 2C_{12})}, \\ S_{44} &= \frac{1}{C_{44}}. \end{aligned} \tag{A2}$$

References

1. Wang, Y.; Gray, D.; Berry, D.; Gao, J.; Li, M.; Li, J.; Viehland, D. An Extremely Low Equivalent Magnetic Noise Magnetoelectric Sensor. *Adv. Mater.* **2011**, *23*, 4111–4114. doi:10.1002/adma.201100773.
2. Gun Lee, D.; Man Kim, S.; Kyung Yoo, Y.; Hyun Han, J.; Won Chun, D.; Kim, Y.C.; Kim, J.; Seon Hwang, K.; Song Kim, T.; Woo Jo, W.; et al. Ultra-sensitive magnetoelectric microcantilever at a low frequency. *Appl. Phys. Lett.* **2012**, *101*, 182902. doi:10.1063/1.4764944.
3. Piorra, A.; Jahns, R.; Teliban, I.; Gugat, J.L.; Gerken, M.; Knöchel, R.; Quandt, E. Magnetoelectric thin film composites with interdigital electrodes. *Appl. Phys. Lett.* **2013**, *103*, 032902. doi:10.1063/1.4812706.
4. Zhai, J.; Xing, Z.; Dong, S.; Li, J.; Viehland, D. Detection of pico-Tesla magnetic fields using magneto-electric sensors at room temperature. *Appl. Phys. Lett.* **2006**, *88*, 062510. doi:10.1063/1.2172706.
5. Schmelz, M.; Stolz, R.; Zakosarenko, V.; Schönau, T.; Anders, S.; Fritzsch, L.; Mück, M.; Meyer, H.G. Field-stable SQUID magnetometer with sub-fT/$Hz^{1/2}$-resolution based on sub-micrometer cross-type Josephson tunnel junctions. *Supercond. Sci. Technol.* **2011**, *24*, 065009. doi:10.1088/0953-2048/24/6/065009.
6. Su, J.; Niekiel, F.; Fichtner, S.; Kirchhof, C.; Meyners, D.; Quandt, E.; Wagner, B.; Lofink, F. Frequency tunable resonant magnetoelectric sensors for the detection of weak magnetic field. *J. Micromech. Microeng.* **2020**, *30*, 075009. doi:10.1088/1361-6439/ab8dd0.
7. Fetisov, L.Y.; Serov, V.N.; Chashin, D.V.; Makovkin, S.A.; Srinivasan, G.; Viehland, D.; Fetisov, Y.K. A magnetoelectric sensor of threshold DC magnetic fields. *J. Appl. Phys.* **2017**, *121*, 154503. doi:10.1063/1.4981533.

8. PourhosseiniAsl, M.J.; Chu, Z.; Gao, X.; Dong, S. A hexagonal-framed magnetoelectric composite for magnetic vector measurement. *Appl. Phys. Lett.* **2018**, *113*, 092902. doi:10.1063/1.5022094.
9. Zhang, J.; Li, P.; Wen, Y.; He, W.; Yang, A.; Lu, C. Packaged current-sensing device with self-biased magnetoelectric laminate for low-frequency weak-current detection. *Smart Mater. Struct.* **2014**, *23*, 095028. doi:10.1088/0964-1726/23/9/095028.
10. Filippov, D.; Firsova, T.; Laletin, V.; Poddubnaya, N. The magnetoelectric effect in nickel–GaAs–nickel structures. *Tech. Phys. Lett.* **2017**, *43*, 313–315. doi:10.1134/S106378501703018X.
11. Spetzler, B.; Kirchhof, C.; Quandt, E.; McCord, J.; Faupel, F. Magnetic Sensitivity of Bending-Mode Delta-E-Effect Sensors. *Phys. Rev. Applied* **2019**, *12*, 064036. doi:10.1103/PhysRevApplied.12.064036.
12. Hui, Y.; Nan, T.; Sun, N.X.; Rinaldi, M. High Resolution Magnetometer Based on a High Frequency Magnetoelectric MEMS-CMOS Oscillator. *J. Microelectromechanical Syst.* **2015**, *24*, 134–143. doi:10.1109/JMEMS.2014.2322012.
13. Kiser, J.; Finkel, P.; Gao, J.; Dolabdjian, C.; Li, J.; Viehland, D. Stress reconfigurable tunable magnetoelectric resonators as magnetic sensors. *Appl. Phys. Lett.* **2013**, *102*, 042909. doi:10.1063/1.4789500.
14. Shen, Y.; Gao, J.; Wang, Y.; Li, J.; Viehland, D. High non-linear magnetoelectric coefficient in Metglas/PMN-PT laminate composites under zero direct current magnetic bias. *J. Appl. Phys.* **2014**, *115*, 094102. doi:10.1063/1.4867516.
15. Gojdka, B.; Jahns, R.; Meurisch, K.; Greve, H.; Adelung, R.; Quandt, E.; Knöchel, R.; Faupel, F. Fully integrable magnetic field sensor based on delta-E effect. *Appl. Phys. Lett.* **2011**, *99*, 223502. doi:10.1063/1.3664135.
16. Kim, H.J.; Wang, S.; Xu, C.; Laughlin, D.; Zhu, J.; Piazza, G. Piezoelectric/magnetostrictive MEMS resonant sensor array for in-plane multi-axis magnetic field detection. 2017 IEEE 30th International Conference on Micro Electro Mechanical Systems (MEMS), 2017, pp. 109–112. doi:10.1109/MEMSYS.2017.7863352.
17. Zhang, Z.; Wu, H.; Sang, L.; Takahashi, Y.; Huang, J.; Wang, L.; Toda, M.; Akita, I.M.; Koide, Y.; Koizumi, S.; et al. Enhancing Delta E Effect at High Temperatures of Galfenol/Ti/Single-Crystal Diamond Resonators for Magnetic Sensing. *ACS Appl. Mater. Interfaces* **2020**, *12*, 23155–23164. doi:10.1021/acsami.0c06593.
18. Krey, M.; Hähnlein, B.; Tonisch, K.; Krischok, S.; Töpfer, H. Automated Parameter Extraction Of ScAlN MEMS Devices Using An Extended Euler-Bernoulli Beam Theory. *Sensors* **2020**, *20*, 1001. doi:10.3390/s20041001.
19. Haehnlein, B.; Kellner, M.; Krey, M.; Nikpourian, A.; Pezoldt, J.; Michael, S.; Toepfer, H.; Krischok, S.; Tonisch, K. The Angle Dependent Δe Effect in Tin/Aln/Ni Micro Cantilevers. Preprint available at SSRN: https://ssrn.com/abstract=4112978.
20. Giallonardo, J.; Erba, U.; Austa, K.; Palumbo, G. The influence of grain size and texture on the Young's modulus of nanocrystalline nickel and nickel-iron alloys. *Philos. Mag.* **2011**, *91*, 4594–4605. doi:10.1080/14786435.2011.615350.
21. Ishizaki, T.; Yatsugi, K.; Akedo, K. Effect of Particle Size on the Magnetic Properties of Ni Nanoparticles Synthesized with Trioctylphosphine as the Capping Agent. *Nanomaterials* **2016**, *6*, 172. doi:10.3390/nano6090172.
22. Hähnlein, B.; Schaaf, P.; Pezoldt, J. Size effect of Young's modulus in AlN thin layers. *J. Appl. Phys.* **2014**, *116*, 124306. doi:10.1063/1.4896496.
23. Hähnlein, B.; Kovac Jr, J.; Pezoldt, J. Size effect of the silicon carbide Young's modulus. *Phys. Status Solidi A* **2017**, *214*, 1600390. doi:10.1002/pssa.201600390.
24. Mandal, S.K.; Sreenivasulu, G.; Petrov, V.M.; Srinivasan, G. Magnetization-graded multiferroic composite and magnetoelectric effects at zero bias. *Phys. Rev. B* **2011**, *84*, 014432. doi:10.1103/PhysRevB.84.014432.
25. Bichurin, M.I.; Petrov, R.V.; Leontiev, V.S.; Sokolov, O.V.; Turutin, A.V.; Kuts, V.V.; Kubasov, I.V.; Kislyuk, A.M.; Temirov, A.A.; Malinkovich, M.D.; et al. Self-Biased Bidomain LiNbO3/Ni/Metglas Magnetoelectric Current Sensor. *Sensors* **2020**, *20*. doi:10.3390/s20247142.
26. Cullity, B.D.; Graham, C.D. *Introduction to magnetic materials*; John Wiley & Sons, 2008; pp. 197–273. doi:10.1002/9780470386323.
27. Carr, W. Invar and volume magnetostriction. *J. Magn. Magn. Mater.* **1979**, *10*, 197–204. doi:10.1016/0304-8853(79)90177-X.
28. Masiyama, Y. On the magnetostriction of a single crystal of nickel. *Sci. Rep. Tohoku Imp. Univ.* **1928**, *17*, 945–961.
29. Spetzler, B.; Golubeva, E.V.; Müller, C.; McCord, J.; Faupel, F. Frequency Dependency of the Delta-E Effect and the Sensitivity of Delta-E Effect Magnetic Field Sensors. *Sensors* **2019**, *19*, 4769. doi:10.3390/s19214769.
30. Rösler, J.; Harders, H.; Bäker, M. *Mechanisches Verhalten der Werkstoffe*; Vieweg+Teubner, 2019; pp. 51–53. doi:10.1007/978-3-658-26802-2.
31. Ledbetter, H.; Reed, R. Elastic Properties of Metals and Alloys, I. Iron, Nickel, and Iron-Nickel Alloys. *J. Phys. Chem. Ref. Data* **1973**, *2*, 531–617. doi:10.1063/1.3253127.
32. Yamamoto, M. The Elastic Constants of Nickel Single Crystals. *J. Jpn. I. Met. Mater.* **1942**, *6*, 331–338. doi:10.2320/jinstmet1937.6.7_331.
33. McCarthy, E.; Bellew, A.; Sader, J.; Boland, J. Poisson's ratio of individual metal nanowires. *Nat. Commun.* **2014**, *5*, 4336. doi:10.1063/1.1702218.
34. Zhou, H.; Pei, Y.; Fang, D. Magnetic Field Tunable Small-scale Mechanical Properties of Nickel Single Crystals Measured by Nanoindentation Technique. *Sci. Rep.* **2014**, *4*, 4583. doi:10.1038/srep04583.
35. Baxy, A.; Sarkar, A. Natural frequencies of a rotating curved cantilever beam: A perturbation method-based approach. Proceedings of the Institution of Mechanical Engineers, Part C: Journal of Mechanical Engineering Science, 2020, Vol. 234, pp. 1706–1719. doi:10.1177/0954406219899117.
36. Greve, H.; Woltermann, E.; Quenzer, H.J.; Wagner, B.; Quandt, E. Giant magnetoelectric coefficients in (Fe90Co10)78Si12B10-AlN thin film composites. *Appl. Phys. Lett.* **2010**, *96*, 182501. doi:10.1063/1.3377908.

37. Lou, J.; Insignares, R.E.; Cai, Z.; Ziemer, K.S.; Liu, M.; Sun, N.X. Soft magnetism, magnetostriction, and microwave properties of FeGaB thin films. *Appl. Phys. Lett.* **2007**, *91*, 182504. doi:10.1063/1.2804123.
38. Yang, P.; Peng, S.; Wu, X.B.; Wan, J.G.; Zhu, J.S. Magnetoelectric study in Terfenol-D/PFNT laminate composite. *Integr. Ferroelectr.* **2008**, *99*, 86–92. doi:10.1080/10584580802107742.
39. Nan, T.; Hui, Y.; Rinaldi, M.; Sun, N.X. Self-Biased 215MHz Magnetoelectric NEMS Resonator for Ultra-Sensitive DC Magnetic Field Detection. *Sci. Rep.* **2013**, *3*, 1985. doi:10.1038/srep01985.
40. Kirchner, H. Über den Einfluß von Zug, Druck und Torsion auf die Längsmagnetostriktion. *Ann. Phys.* **1936**, *419*, 49–69. doi:10.1002/andp.19364190105.
41. Ludwig, A.; Quandt, E. Optimization of the Delta-E effect in thin films and multilayers by magnetic field annealing. *IEEE Trans. Magn.* **2002**, *38*, 2829–2831. doi:10.1109/TMAG.2002.802467.
42. Coey, J.M. *Magnetism and magnetic materials*; Cambridge university press, 2010; pp. 264–304. doi:10.1017/CBO9780511845000.
43. Ciria, M.; Arnaudas, J.I.; Benito, L.; de la Fuente, C.; del Moral, A.; Ha, J.K.; O'Handley, R.C. Magnetoelastic coupling in thin films with weak out-of-plane anisotropy. *Phys. Rev. B* **2003**, *67*, 024429. doi:10.1103/PhysRevB.67.024429.
44. Li, M.; Matyushov, A.; Dong, C.; Chen, H.; Lin, H.; Nan, T.; Qian, Z.; Rinaldi, M.; Lin, Y.; Sun, N.X. Ultra-sensitive NEMS magnetoelectric sensor for picotesla DC magnetic field detection. *Appl. Phys. Lett.* **2017**, *110*, 143510. doi:10.1063/1.4979694.
45. Liang, X.; Dong, C.; Chen, H.; Wang, J.; Wei, Y.; Zaeimbashi, M.; He, Y.; Matyushov, A.; Sun, C.; Sun, N. A Review of Thin-Film Magnetoelastic Materials for Magnetoelectric Applications. *Sensors* **2020**, *20*. doi:10.3390/s20051532.
46. Spetzler, B.; Golubeva, E.V.; Friedrich, R.M.; Zabel, S.; Kirchhof, C.; Meyners, D.; McCord, J.; Faupel, F. Magnetoelastic Coupling and Delta-E Effect in Magnetoelectric Torsion Mode Resonators. *Sensors* **2021**, *21*. doi:10.3390/s21062022.
47. Durdaut, P.; Rubiola, E.; Friedt, J.M.; Müller, C.; Spetzler, B.; Kirchhof, C.; Meyners, D.; Quandt, E.; Faupel, F.; McCord, J.; et al. Fundamental Noise Limits and Sensitivity of Piezoelectrically Driven Magnetoelastic Cantilevers. *J. Microelectromechanical Syst.* **2020**, *29*, 1347–1361. doi:10.1109/JMEMS.2020.3014402.
48. Namazu, T.; Inoue, S.; Takemoto, H.; Koterazawa, K. Mechanical Properties of Polycrystalline Titanium Nitride Films Measured by XRD Tensile Testing. *IEEJ Transactions on Sensors and Micromachines* **2005**, *125*, 374–379. doi:10.1541/ieejsmas.125.374.
49. Webster, W.L. Magnetostriction and change of resistance in single crystals of iron and nickel. *Proc. Phys. Soc.* **1930**, *42*, 431–440. doi:10.1088/0959-5309/42/5/311.
50. Daniel, L. An analytical model for the magnetostriction strain of ferromagnetic materials subjected to multiaxial stress. *Eur. Phys. J. Appl. Phys.* **2018**, *83*, 30904. doi:10.1051/epjap/2018180079.